A portable x-ray source with a nanostructured Pt-coated silicon field emission cathode for absorption imaging of low-Z materials

Anirban Basu[1]**, Michael E Swanwick**[1]**, Arash A Fomani**[1] **and Luis Fernando Velásquez-García**

Microsystems Technology Laboratories, Massachusetts Institute of Technology, Cambridge MA 02139, USA

E-mail: anirbasu@mit.edu and Velasquez@alum.mit.edu

CrossMark

Abstract

We report the design, fabrication, and characterization of a portable x-ray generator for imaging of low-atomic number materials such as biological soft tissue. The system uses a self-aligned, gated, Pt-coated silicon field emitter cathode with two arrays of 62 500 nano-sharp tips arranged in a square grid with $10\,\mu$m emitter pitch, and a natural convection-cooled reflection anode composed of a Cu bar coated with a thin Mo film. Characterization of the field emitter array demonstrated continuous emission of 1 mA electron current ($16\,\mathrm{mA\,cm^{-2}}$) with >95% current transmission at a 150 V gate-emitter bias voltage for over 20 h with no degradation. The emission of the x-ray source was characterized across a range of anode bias voltages to maximize the fraction of photons from the characteristic K-shell peaks of the Mo film to produce a quasi-monochromatic photon beam, which enables capturing high-contrast images of low-atomic number materials. The x-ray source operating at the optimum anode bias voltage, i.e. 35 kV, was used to image *ex vivo* and nonorganic samples in x-ray fluoroscopic mode while varying the tube current; the images resolve feature sizes as small as ~160 μm.

Keywords: field emission, medical imaging, silicon field emitter array, x-ray generation

(Some figures may appear in colour only in the online journal)

1. Introduction

X-rays, discovered over a century ago [1], are widely used in applications such as healthcare, airport security, crystallography [2], spectroscopy [3] and microfabrication [4]. In a traditional x-ray source electrons are accelerated using a multi-kilovolt bias voltage to then be slowed down by colliding with a dense material, producing ionizing radiation [5]. In many applications the size and weight of the x-ray source is not as important as other specifications such as photon flux, photon energy, stability, and reliability during long-term operation. However, smaller x-ray sources are a good fit when the target areas are small [6] or when the smaller dimensions and weight of the x-ray source enables desirable capabilities such as compactness or portability. For example, compact x-ray sources can revolutionize computerized tomography (CT) by making possible the implementation of a system with multiple x-ray sources that provides a wide range of information with reduced movement of the gantry [7].

Arguably, the most critical component of the x-ray source is the cathode because it is the driver of the process; the cathode supplies the electrons that produce the x-rays, and sets the time response of the overall system. State-of-the-art cathodes for x-ray sources are thermionic, that is, they 'boil-off' electrons from a glowing filament. Thermionic cathodes are reliable and can steadily produce high currents; however,

[1] A Basu, M Swanwick, and A Fomani equally contributed to this work.

a portable x-ray source would benefit from having a cathode that is more resilient to lower vacuum, compatible with operation in environments with traces of reacting gases, and capable of faster switching. Field emission electron sources, based on quantum tunneling of electrons into vacuum due to high surface electrostatic fields [8], are an attractive alternative to thermionic cathodes that fulfills these criteria. Field emission cathodes utilize sharp tips to produce high electric fields at low voltage, and typically involve a plurality of tips to increase and uniformize the emission. Field emission cathodes also consume less power than thermionic emitters [6], although this is not an important advantage for portable x-ray systems as most of the power dissipation occurs in the anode. Examples of reported field emission cathodes for x-ray sources include silicon [9, 10] and carbon nanotube (CNT) emitter arrays [11–13].

Compared to CNT-based cathodes, arrays of single-crystal, gated silicon tips are capable of producing higher current at lower voltages because the geometry of the emitter (height, tip diameter, orientation of the tip with respect to the substrate) can be controlled better [9, 14, 15], which makes possible the fabrication with high yield of self-aligned proximal gates for large emitter arrays [16]; in addition, regulation of the current produced by each emitter can be achieved using the semiconductor material [17, 18]. Lack of control in the CNT growth can also lead to cathode-gate shorting, resulting in higher gate leakage and reduction of the power efficiency of the cathode [19]. Good uniformity of the tip radius across a field emitter array (FEA) is highly desirable because field emitted currents depend exponentially on the inverse of the tip radius and therefore, the variation on the tip radius across the array results in emission non-uniformity and array subutilization [17]. Self-aligned, gated Si FEAs can turn on with as little as 30 V and emit mA-level current with 80 V emitter-gate bias voltage [16], compared to CNT cathodes that emit μA-level current at 300 V and require >600 V emitter-gate bias voltage to produce mA-level current [19]; in this work, 1 mA current emission from a 62 500-FEA is demonstrated with <150 V emitter-gate bias voltage.

The other critical component of an x-ray source is the anode because it is the structure that generates the x-rays. For reliability and vacuum compatibility, the anode must have a high melting temperature of at least 1000 K and should have moderate outgassing at a high temperature. There are two types of x-ray anodes, i.e. a transmission anode and reflection anode, depending on the direction of the x-rays used for imaging compared to the direction of the electron beam. In a transmission anode, the x-ray beam that is used for imaging comes from the back of the anode in the same direction of the electron beam, whereas in a reflection anode the x-ray beam comes from the surface directly hit by the electron beam and the two beams are roughly perpendicular to each other. Transmission anodes pose several advantages over reflection anodes, e.g. they are less affected by the so-called heel effect, i.e. a gradient in the intensity of the x-ray beam due to absorption of photons by the anode material with the larger intensity of the beam located toward the cathode, which generates images with spatial non-uniformity.

We previously reported a tabletop x-ray source with a field emission cathode and a transmission anode that used a beryllium wafer coated with a thin Au film as x-ray generating material [10]. The cathode was composed of 10 independent arrays of 490 2.5 μm-tall, 5 nm-tip radius, single-crystal silicon tips with a 1.5 μm-thick gate oxide layer and a 500 nm-thick n-doped polysilicon gate with a 0.6 μm diameter self-aligned aperture. At a given time, only one array was used to emit electrons; the plurality of arrays provided cathode redundancy and was intended to increase the reliability of the x-ray source. The x-ray source was used to capture detailed absorption images of *ex vivo* samples. However, the x-ray source reported in [10] suffered from operational issues due to inadequate heat dissipation of the anode, resulting in short cathode life due to back-ion bombardment caused by the lower vacuum that ensued from the anode outgassing. In this work, the x-ray source uses a cathode composed of 2 independent arrays of 62 500 Pt-coated, 2.5 μm-tall, 5 nm-tip radius, single-crystal silicon tips with a 2.5 μm-thick SiO_x/SiN_y gate dielectric layer and a nano-thick Pt film gate with 3 μm diameter self-aligned aperture; the array size is more than two orders of magnitude larger than the array size of the chip cathode reported in [10], requiring to produce a lot less current from each emitter to deliver the same current, which greatly improves the reliability of the cathode. In addition, in this work the source uses a Cu rod coated with a 5 μm-thick Mo film to generate x-rays—a natural convection-cooled reflection anode with a larger thermal mass that addresses the cooling problems of the previous design.

An x-ray source produces ionizing radiation in two different ways: 1) the deceleration of high-energy electrons by collision with the dense anode material produces polychromatic photons known as bremsstrahlung x-rays; 2) the electronic transitions of the anode material can also generate x-rays of a few specific frequencies, with intensities related to the frequency of the photons, the anode bias voltage, and the yield of the process. While polychromatic x-rays are widely used in most x-ray systems, it has been recognized that monochromatic x-rays can be used to capture better images [20] because every x-ray detector has an optimal energy level that maximizes its efficiency. However, implementing a truly monochromatic, portable x-ray source is challenging. Synchrotron sources for CT such as those described in [21, 22] are bulky, while other attempts using a filtration technique [23] or additional optical components such as mirrors and lenses [24, 25] are either inefficient or complicated. The best results for monochromatic x-rays have been achieved by maximizing the contribution from the characteristic peaks of the target anode as described in [10, 26]. Although the K-shell peak from Au and L-shell peak from Mo can be used for imaging, the K-shell peak from Mo has a higher energy than either of the two. The ratio of the Mo K-shell peak to the bremsstrahlung radiation can be optimized by adjusting the anode bias voltage.

An important parameter of an x-ray source for imaging is the number of x-ray photons available during exposure. Photon counting detectors are often used for measuring the total number of photons during exposure [27]. Doses in CT have been characterized and described in [28, 29]. In this

J. Phys. D: Appl. Phys. 48 (2015) 225501

A Basu et al

work, a small portable CdTe detector was used to obtain an estimate of the photo flux from the x-ray source. The ability to meaningfully calibrate an x-ray source using this technique is discussed in [30]. CdTe detectors are relatively inexpensive compared to photon counting detector panels and can be calibrated first with a radioactive source and then used for characterizing x-ray generation.

2. Description of the x-ray source

The x-ray source, shown in figure 1, is mounted on an optical breadboard and uses a 2.75-inch spherical cube as vacuum chamber with ~200 cm^3 of internal space. The faces of the cube interface with the following hardware: (i) a custom-made high-voltage electrical feedthrough connected to the reflection anode, i.e. a 0.5 in diameter Cu bar with the end inside the chamber cut at 15°, coated with a 5 μm-thick Mo film; (ii) a beryllium window for transmission of x-rays outside the vacuum chamber; (iii) a 4-port SHV-5 electrical feedthrough to interface with the cathode chip; (iv) a 25 l s^{-1} ion pump connected to the chamber by a gate valve; (v) a glass window for visual inspection of the setup inside the vacuum chamber; and (vi) a gate valve to pump down the vacuum chamber until the pressure is low enough to activate the ion pump. The cathode chip has a custom-made holder (figure 2) with a stainless steel spring clip, isolated from the rest of the baseplate by a ceramic spacer, which connects one of the gate electrodes of the chip to one of the ports of the SHV-5 feedthrough. The electrical connection to the chip substrate was made directly through the baseplate, which is connected to another of the ports of the SHV-5 feedthrough. The cathode and the anode are placed on opposite flanges, while the x-ray window is at right angles to both. The ion pump maintains a base vacuum level of 10^{-10} Torr. The source weighs approximately 35 lbs. including the weight of the ion pump but without including the weight of the power supplies. The x-ray source uses a mix of standard and custom vacuum parts; further optimization of the chamber can greatly reduce its weight and size. Two power supplies were used during the characterization of the x-ray source, i.e. the substrate of the chip was biased at a negative voltage using a Stanford Research Systems PS350 power supply that can deliver between 50 V and 5 kV, the anode voltage was supplied by a Matsusada high voltage power supply that can deliver 1–120 kV, and the gate electrode of the cathode chip was connected to the common ground.

The field emission chip used in this work is based on the technology reported in [31], which is capable of generating 1.1 A cm^{-2} at a gate-emitter bias voltage of 300 V. The chip used in the x-ray source has two arrays of 62 500 emitters (i.e. two 250 × 250 emitter arrays) with 10 μm emitter pitch; the arrays can be independently actuated and are meant to provide redundancy to the cathode to improve the reliability of the source. An SEM of a small cluster of emitters part of a 62 500-FEA and a cross-section schematic of a field emission diode are shown in figure 3. Each emitter diode consists of a tip with 5 nm radius, surrounded by a gate aperture that is self-aligned, i.e. symmetric about the axis of the emitter tip. A 2.5 μm-thick SiO$_x$/SiN$_y$ dielectric film stack separates the

chip substrate from the gate electrode, which is a thin Pt film; the Pt film also covers the tip to protect it from back-ion sputtering. The nano-sharp tip generates a high electric field on its surface when a bias voltage is applied between the gate and the emitter. A thick gate dielectric is necessary so that it does not breakdown when a high electric field is applied across it during operation; the electric field in the dielectric should be a fraction of its breakdown field, which is approximately 500 V μm^{-1} for SiO$_2$ deposited using the plasma-enhanced chemical vapor deposition (PECVD) technique followed by annealing [32]. The breakdown field of the Si-rich SiN$_y$ is dependent on the concentration of Si and can vary from 250 to 1,200 V μm^{-1} [33].

A schematic of the fabrication process flow of the cathode chip is shown in figure 4. The process flow uses an *n*-type, single-side-polished, single-crystal, 150 mm silicon wafer as substrate. First, 3 μm-tall pillars are etched on the substrate using reactive-ion etching (RIE) with HBr/Cl$_2$ chemistry and a photoresist mask transferred with projection lithography (figure 4(a)). Next, a 3 μm-thick PECVD SiO$_x$ film is deposited on top of the pillars; the substrate is then annealed at 1000 °C for 3 h to improve the mechanical and electrical properties of the film, followed by a chemical mechanical polishing (CMP) step that removes the oxide film down to the level of the pillars (figure 4(b)). Then, a 0.2 μm-thick thermal oxide film is grown (figure 4(c)). After that, a low-pressure chemical vapor deposited (LPCVD) SiN$_y$ film is deposited over the oxide film, and the SiN$_y$ film is patterned with the gate aperture features using RIE with SF$_6$ chemistry and a photoresist mask transferred with projection lithography (figure 4(d)). Another projection lithography is performed, this time with the features that define emitter caps slightly smaller than the diameter of the pillar, concentric to slightly larger gate aperture features; the mask is transferred to the film stack using RIE with a CF$_4$ chemistry (figure 4(e)). The process continues by isotropically etching the pillars using RIE with an SF$_6$ chemistry; the step creates partially sharpened tips with the oxide caps attached (figure 4(f)). For completing the sharpening of the tips, a dry oxidation step is performed (figure 4(g)), and the oxide film and oxide caps are etched away using buffered oxide etch (BOE). Finally, a thin Pt film is deposited using e-beam evaporation to create the gate electrode right on top of the SiN$_y$ film; the Pt film also coats the tips and makes them more resilient (figure 4(h)).

3. Characterization of the cathode

Electrical characterization of the cathode chip in a triode configuration was performed in a separate ultra-high vacuum chamber where the base pressure is maintained at <5 × 10^{-10} Torr. A tungsten probe was used to make contact to the gate electrode while the sample holder was used to bias a voltage to the chip substrate, i.e. emitters. The anode, i.e. collector, is a stainless steel cylinder suspended right in front of the active area of the chip. Source-measuring units (SMUs) Keithley 2657A were used to bias voltages to the anode, cathode and gate electrode, and to measure currents. Two kinds of experiments were performed to characterize the
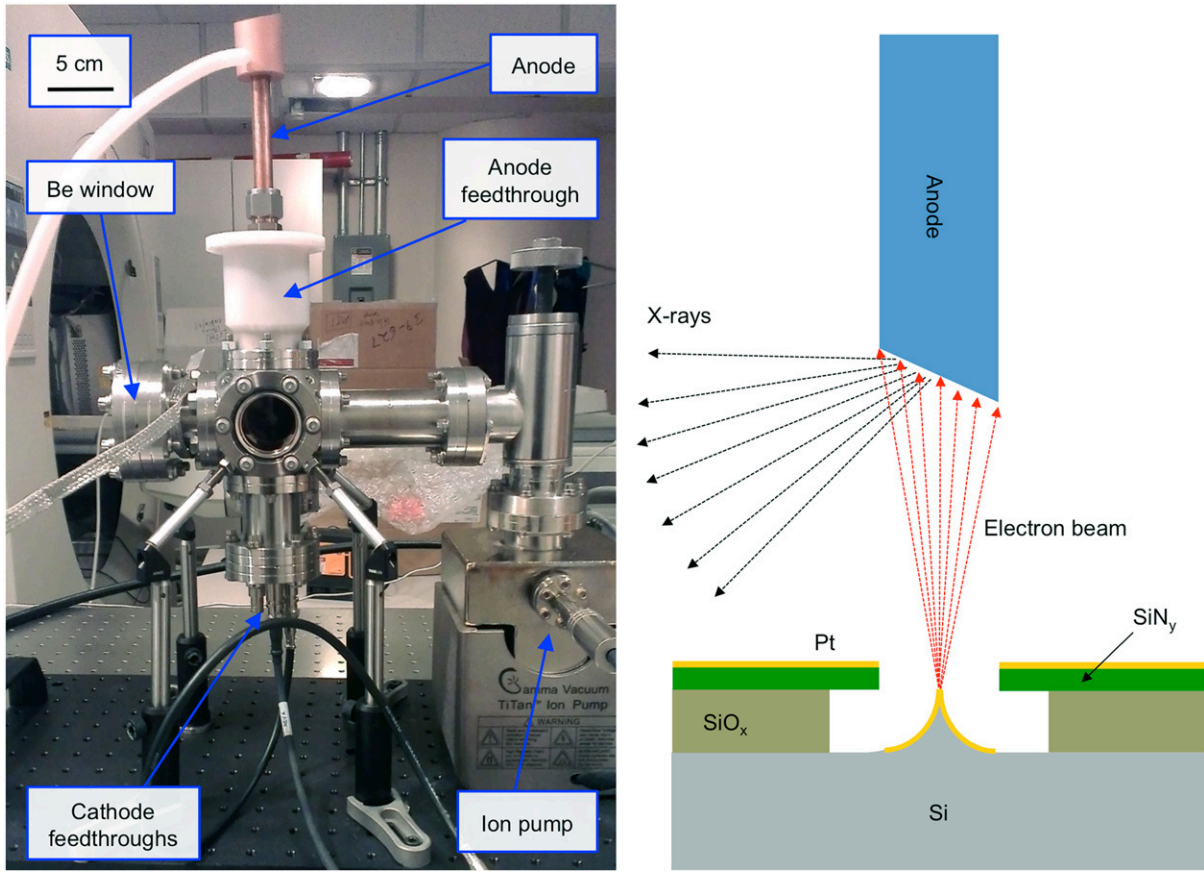
J. Phys. D: Appl. Phys. 48 (2015) 225501

A Basu *et al*

Figure 1. Portable x-ray source: assembled system (left) and schematic (right).
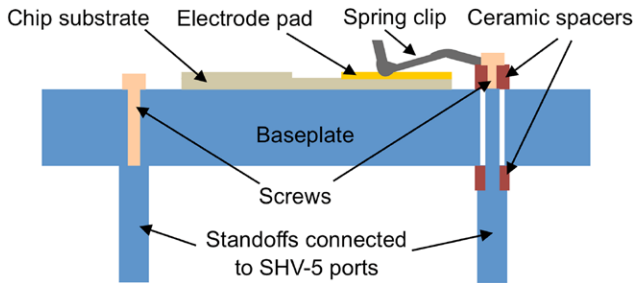

Figure 2. Schematic of the chip holder.

chips. In the first kind of experiments, the gate electrode was biased at 0V, the emitter substrate was biased at a negative voltage between 0V and 120V, and the collector was biased at +1000V; typical current–voltage (*I–V*) characteristics collected in these experiments are shown in figure 5. Startup voltages as low as 32V were measured. For gate-to-emitter bias voltages below 40V, the gate current is dominated by leakage through the dielectric; the gate current reduces to about 0.1% of the emitter current when the gate-to-emitter bias voltage is above 80V. For bias voltages above 117V, mA-level currents were produced.

In a field emitter the current density *J* is given by [34, 35]

$$J = a_{FN}F^2 \exp\left(-\frac{b_{FN}}{F}\right) \qquad (1)$$

Where

$$a_{FN} = \frac{A}{1.1\Phi} \exp\left(\frac{10.4}{\Phi^{1/2}}\right) \qquad (2)$$

and

$$b_{FN} = 0.95B\Phi^{3/2} \qquad (3)$$

where *F,* in V.cm^{-1}, is the surface electric field at the emitter tip, *Φ*, in eV, is the workfunction of the material of the tip surface (in this case Pt), and *A* and *B* are constants equal to 1.54×10^{-6} A.eV.V^{-2} and 6.83×10^7 eV$^{-1.5}$.V.cm^{-1}, respectively. The local electric field *F* is related to the gate-to-emitter bias voltage V_{GE} by $F = \beta V_{GE}$ where β is the field factor, approximately equal to $3.82 \times 10^6 R_{tip}^{-0.89}$ cm^{-1} from simulations of the electric field generated by the emitter diode using finite element analysis, where R_{tip} is the tip radius in nanometers. Therefore, the current field emitted *I* from a tip with emitting surface area *α*, in cm^2, is

$$I = \alpha \frac{1.4 \times 10^{-6}}{\Phi} \exp\left(\frac{10.4}{\Phi^{1/2}}\right) \beta^2 V_{GE}^2 \exp\left(-\frac{6.49 \times 10^7 \Phi^{3/2}}{\beta V_{GE}}\right) \qquad (4)$$

From equation (4), field emitted current describes a straight line with slope $-b_{FN}/\beta$ when plotted as $\ln(I/V_{GE}^2)$ versus V_{GE}^{-1}. Analysis of the collector current shows that the current is field emitted (figure 6). From the slope of the Fowler-Nordheim plot, a field factor equal to 2.46×10^6 cm^{-1} is obtained using 6.35 eV as the workfunction of Pt. From the field factor, an
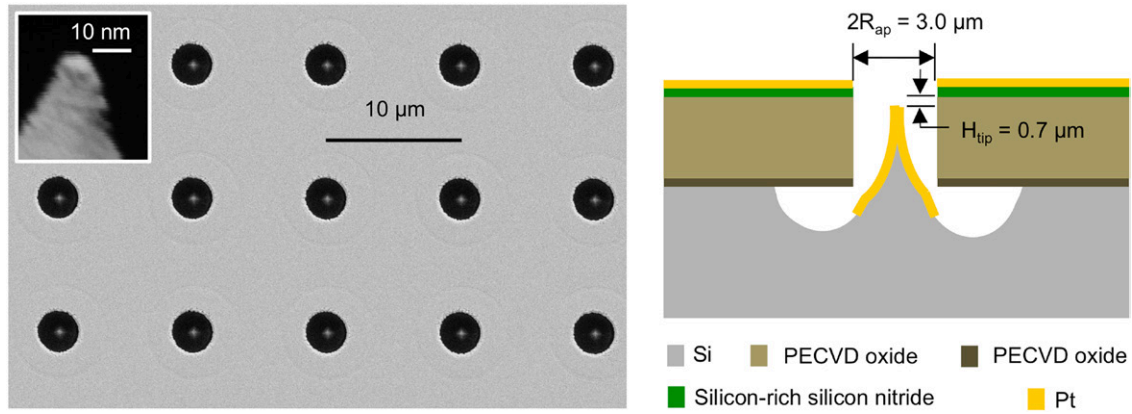
Figure 3. Cluster of self-aligned, gated, Pt-coated silicon field emitter arrays with close-up of an emitter tip (left); cross-section schematic of field emitter diode (right). R_{ap} is the aperture radius, and H_{tip} is the vertical separation between the tip and the bottom of the nitride film.
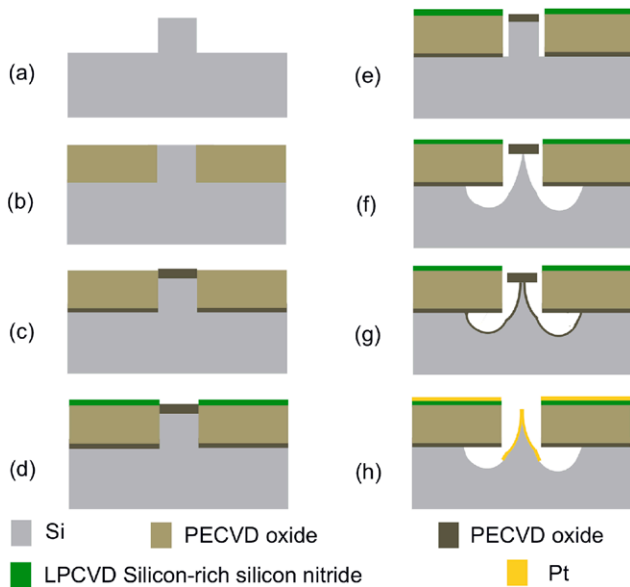

Figure 4. Schematic of process flow to fabricate field emitter array: (*a*) Si pillar formation; (*b*) SiO_x deposition by PECVD followed by planarization using CMP; (*c*) thermal growth of SiO_2; (*d*) silicon-rich silicon nitride deposition by LPCVD and aperture patterning; (*e*) gate dielectric stack patterning and oxide cap formation; (*f*) Si isotropic etching for tip formation; (*g*) tip sharpening by thermal oxidation; (*h*) emitter release and Pt deposition.

Figure 5. *I–V* characteristics of a FEA chip used in the x-ray source. The gate-emitter bias was swept from 0–120 V at 1 V steps in both directions while recording the emitter, gate and collector currents. There is hysteresis in the data as commonly occurs with field emission data.

Figure 6. Fowler–Nordheim plot of the collector current data shown in figure 5.

estimated emitter tip radius of 1.64 nm is obtained, which is on the same order of magnitude of the tip shown in figure 3.

The second kind of experiments entailed verifying that the chip can be continuously operated for periods of time orders of magnitude longer than the typical exposure time to capture an image (tens of seconds). In this case, the emitter current was set at 1 mA using current control on the SMU connected to the substrate, while the bias voltage of the gate electrode was set at 0 V and the bias voltage of the collector was set at +1000 V. The cathode operated continuously for almost 20 h (figure 7); the chip did not die during the test. During the first hours, the collector current fell because the gate leakage increased; however, after 5 h of continuous operation the level of the collector current restored itself to eventually reach >95% of the emitter current and stay like that for the rest of the experiment. The gate-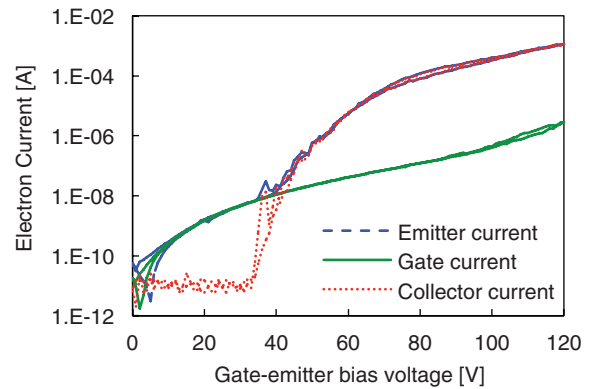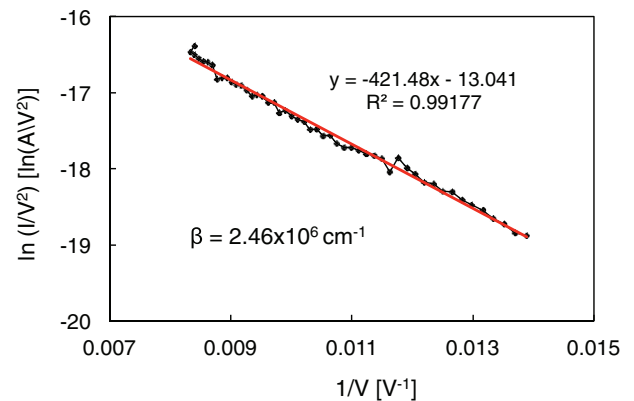emitter bias voltage required to maintain the emission current at 1 mA decreased during this time, finishing at 143 V. The initial increase in gate current is possibly due to defect states present in the dielectric, leading to charge trapping within those defects [36]; as the defect states get filled, there is a reduction in the rate of charge trapping, and consequently, a reduction in gate leakage.
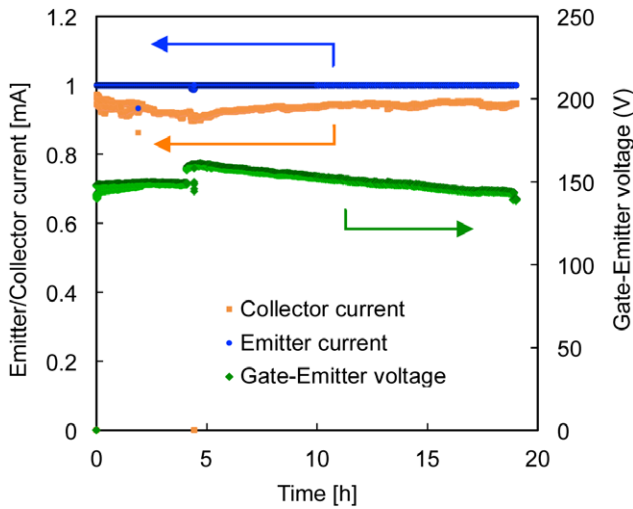
J. Phys. D: Appl. Phys. 48 (2015) 225501

A Basu *et al*

Figure 7. Emitter current, collector current, and gate-to-emitter bias voltage versus time for constant 1 mA emitter current.
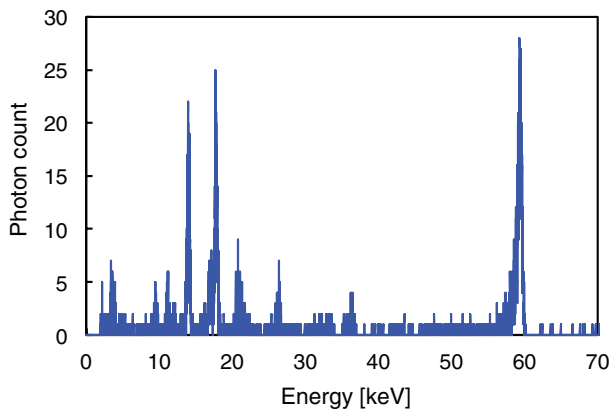

Figure 8. Am^{241} spectrum with calibrated energy axis.

4. Characterization of the photon emission of the x-ray source

The x-rays from the source were characterized using an Amptek X-1-2-3 CdTe spectrometer following a technique similar to that described in [30]. Before characterizing the emission from the x-ray source, the spectrometer output, i.e. photon count at a given photon energy, was calibrated using a sealed Am^{241} source; the result of calibrating the data from the Am^{241} source as captured by the spectrometer at a distance of 1.75 cm and exposure for 10 min is shown in figure 8.

Measuring the photon count from the x-ray source involved two stages of calibration, i.e. estimating the intrinsic and extrinsic efficiencies. The extrinsic efficiency is a measure of the fraction of the total number of photons generated by the source that reach the spectrometer–a function of the location of the source with respect to the detector. The intrinsic efficiency is the fraction of photons, out of those that reach the spectrometer, that are measured by the detector. The 60 keV gamma rays from the Am^{241} sample were used for measuring the intrinsic efficiency; in the case of the spherical Am^{241} source used for calibration, it can be assumed that photons are generated uniformly radially. The total number of 60 keV
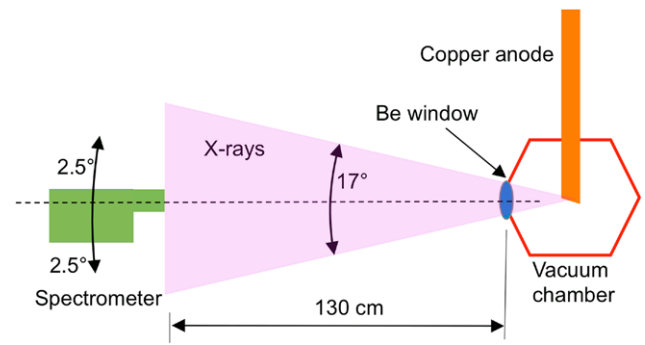

Figure 9. Schematic of the test setup used to collect the data to estimate the extrinsic efficiency and x-ray photon count.
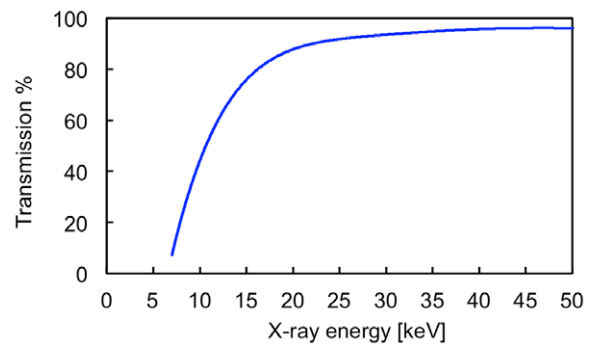

Figure 10. Transmission efficiency versus photon energy for x-rays through 0.25 mm of Be and 130 cm of air.

photons generated by Am^{241} in all directions is estimated by its decay rate; the sealed source of Am^{241} was rated for a radiation of 0.1 μCi out of which 48.19% is γ radiation at 60 keV. This implies that approximately 1,370 60 keV γ photons per second are released in all directions. Thereafter, depending on the position of the source, the fraction of the total number of photons that should reach the detector is estimated. This fraction will be equal to the ratio between the solid angle subtended by the active area of the detector (9 mm^2) and the 4π solid angle of the Am^{241} source. The source-to-detector distance was varied in order to get multiple values of the intrinsic efficiency that should be approximately equal. From these measurements we estimate the intrinsic efficiency of the spectrometer at 97%.

The following considerations were made to estimate the extrinsic efficiency. Initially, the semiangle of the x-ray cone transmitted by the Be window was measured using the circular projection of the emitted x-ray beam on a CsI detector; the projections were captured at different distances from the source. From these projections, it was found that the x-ray cone roughly has a semi-angle of 8.5° which is equivalent to a solid angle of 0.069 sr. The x-ray spectrum was then captured with the CdTe spectrometer placed 130 cm away from x-ray source making an angle of −2.5°, 0° and +2.5° with the axis of the x-ray cone. An average spectrum from these three positions was used for calculating the efficiency in order to account for the heel effect. At a distance of 130 cm, the active area of the spectrometer subtends a solid angle of 2.87×10^{-6} sr. This gives us an extrinsic efficiency of 4.16×10^{-5}. Figure 9
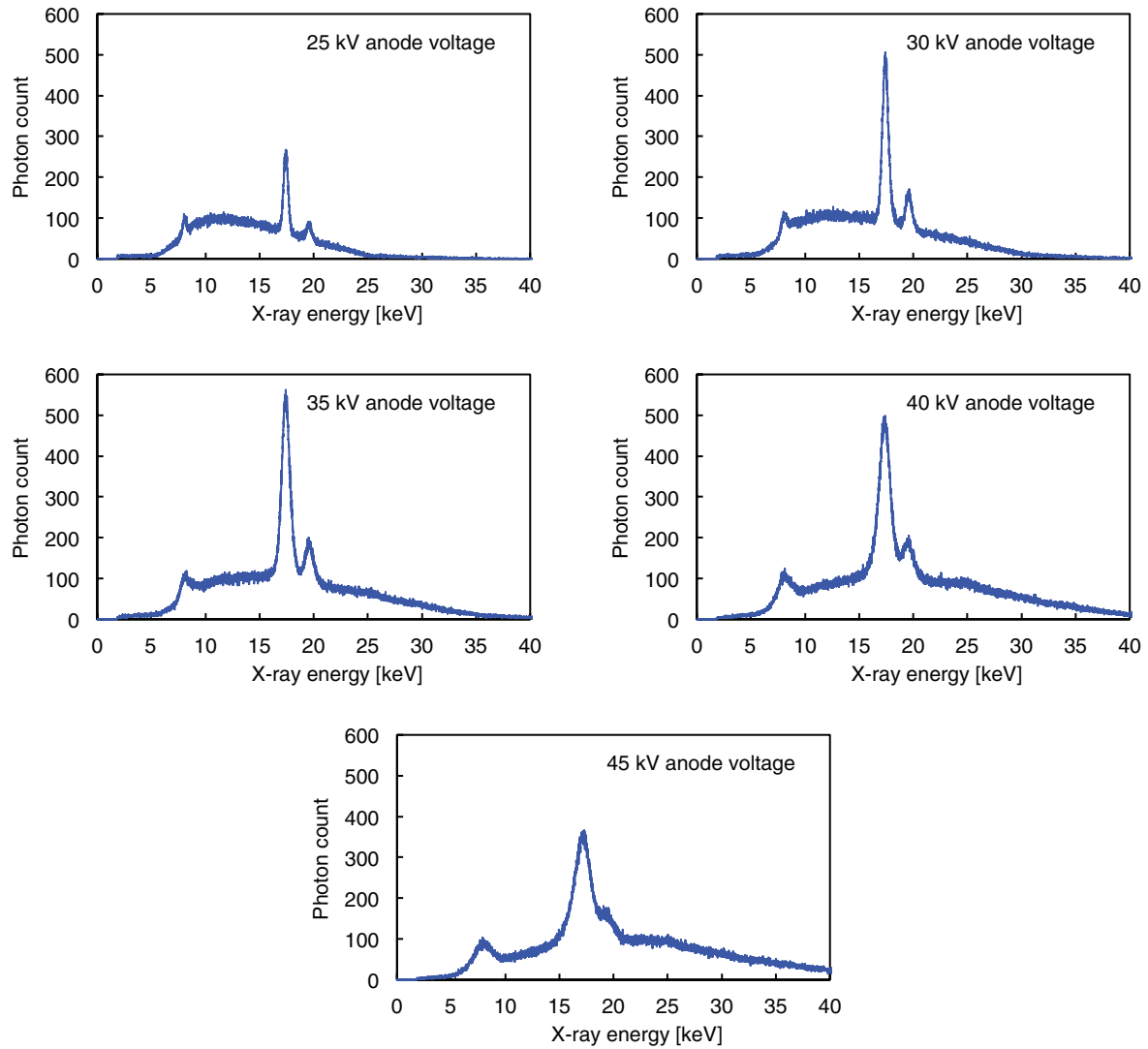
Figure 11. Spectral data for x-rays emitted at different anode bias voltages with an integration time of 5 s.
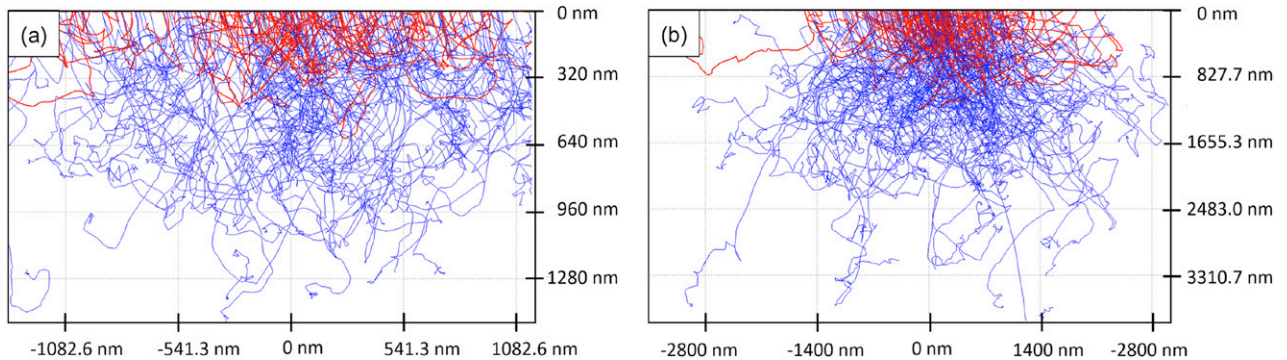

Figure 12. Simulated trajectories of 200 electrons at an anode voltage of (*a*) 25 kV, (*b*) 45 kV. The trajectories in red are electrons that eventually escape from the anode, while the trajectories in blue are electrons that stay within the anode material after slowing down.

shows a schematic (not drawn to scale) of the setup used to collect the data to estimate the extrinsic efficiency and x-ray photon count.

Besides the intrinsic and extrinsic efficiencies, x-rays have a transmission efficiency dependent on the energy of the photons, the media of transmission (in this case air

and beryllium), and the distance traveled in each medium [37]. A graph of effective transmission efficiency versus x-ray energy for the setup used in this work is shown in figure 10. The beryllium window has a thickness of 0.25 mm while the separation between source and detector is 130 cm. Therefore, for x-ray photons with 25 keV energy, accounting

J. Phys. D: Appl. Phys. **48** (2015) 225501

A Basu *et al*

Table 1. Estimated x-ray photons/second from bremsstrahlung and characteristic peaks of the x-ray spectrum when anode current is 15 μA.

Energy (keV)	Bremsstrahlung	K_α-shell Cu peak	K_α-shell Mo peak	Percentage of K_α-shell Mo peak in total photon flux
25	7.76×10^9	9.52×10^8	1.9×10^9	17.90%
30	1.16×10^{10}	1.06×10^9	3.8×10^9	23.09%
35	1.45×10^{10}	1.06×10^9	5.09×10^9	24.65%
40	1.78×10^{10}	1.07×10^9	5.49×10^9	22.54%
45	1.94×10^{10}	8.88×10^8	4.58×10^9	18.42%

Table 2. Tube current and corresponding K_α-shell Mo peak dosage for a 60 s exposure at 35 kV anode voltage.

Tube current (μA)	Number of x-ray photons
150	3.05×10^{12}
200	4.06×10^{12}
250	5.08×10^{12}
330	6.70×10^{12}
400	8.12×10^{12}
450	9.15×10^{12}

for the extrinsic efficiency, together with a transmission efficiency of 91.5%, only 1 part in ~27 087 interacts with the spectrometer.

X-ray spectra were collected using a cathode current of 15 μA while varying the anode bias voltage between 25 kV and 45 kV (figure 11). The spectra shown are the raw data collected from the spectrometer before correcting for the intrinsic efficiency, extrinsic efficiency and attenuation. Two large peaks corresponding to the K_α-shell and K_β-shell transitions of molybdenum appear at approximately 17.4 and 19.4 keV respectively. A smaller peak at 8.6 keV corresponds to the K_α-shell transition of copper; this peak could be caused by direct access of the electrons to the copper rod due to a discontinuous molybdenum film, or it could also be the result of the electrons getting through the molybdenum film and interacting with the copper right underneath. Simulations of the interaction of the electrons with the anode structure (a 5 μm-thick molybdenum film on top of a copper substrate) were conducted using the Monte Carlo software CASINO [38] in order to ascertain the likelihood of electrons reaching the bulk copper after penetrating the molybdenum layer. Shown in figure 12 are the trajectories of electrons at two different energy levels. It was found that for an anode voltage of 45 kV, the electrons are not likely to go deeper than 3.2 μm while for an anode voltage of 25 kV, it can penetrate a depth of only about 1.2 μm. Therefore, we believe the molybdenum film has voids or is cracked, giving direct access of the copper material to the electrons. The 8.6 keV peak was unintended; however, fortunately, it does not significantly affect the properties of the x-ray source for capturing low-Z images as it is of lower energy and less intensity compared to the molybdenum peaks.

Using an intrinsic efficiency equal to 97% and an extrinsic efficiency equal to 4.16×10^{-5}, as previously estimated, and also correcting for the attenuation at different energy levels of the spectrum, the total photon production during 5 s

is 5.31×10^{10} photons, or 1.06×10^{10} photons s^{-1} for the spectral data for 25 kV. By subtracting the photon count due to the Mo and Cu peaks from the overall photon count, we can derive the photon count due to the bremsstrahlung component of the spectrum. We used a $\pm$ 1 keV window around each peak to estimate the photon count produced by the peak, which effectively included the bremsstrahlung radiation within the energy window as part of the photon count; however, the error introduced by this approximation is small.

Table 1 shows the photon count per second for the bremsstrahlung and the characteristic peaks of the x-ray spectrum at different anode voltages when current is set at 15 μA. In the data shown, attenuation in the Be window and in air are both accounted for. For the polychromatic bremsstrahlung component, the attenuation will vary depending on the energy of the x-ray photons. Data from figure 10 has been used to implement this correction. Table 2 shows the dosage for different values of anode current at an energy of 35 keV in terms of number of photons emitted from the x-ray source. Only the K_α-shell Mo peak (17.5 keV) has been counted in the table, although there will be contributions from Cu peak and bremsstrahlung in the total photon count. As expected, there is a linear relationship between the dose and the cathode current.

5. Absorption images using the x-ray source

Shown in figure 13 are images of a computer mouse for a cathode current of 200 μA and anode bias voltage between 25 and 50 kV. These images are fluoroscopic and were captured by exposing the sample for 60 s at 2 frames s^{-1} and then averaging all the captured frames. The image sensor used is a CsI detector made by Varian (PaxScan 4030 CB) with a pixel pitch of 194 μm and a fill factor of 70%. As the anode bias voltage increases, the brightness and the contrast of the image also increase; this is due to the overall larger production of photons for larger anode bias voltage, in particular the production of high-energy photons from the fluorescence of the anode material. The absorption image captured using 35 kV anode bias voltage has better contrast than the images captured with lower and higher anode bias voltage; in particular, the absorption image captured with an anode bias voltage of 50 kV has more brightness but not better contrast. The set of images together with the spectral data in figure 11 suggest a correlation of contrast with the ratio of the characteristic peaks rather than the bremsstrahlung component of the x-rays. Based on the data shown it table 1 it is
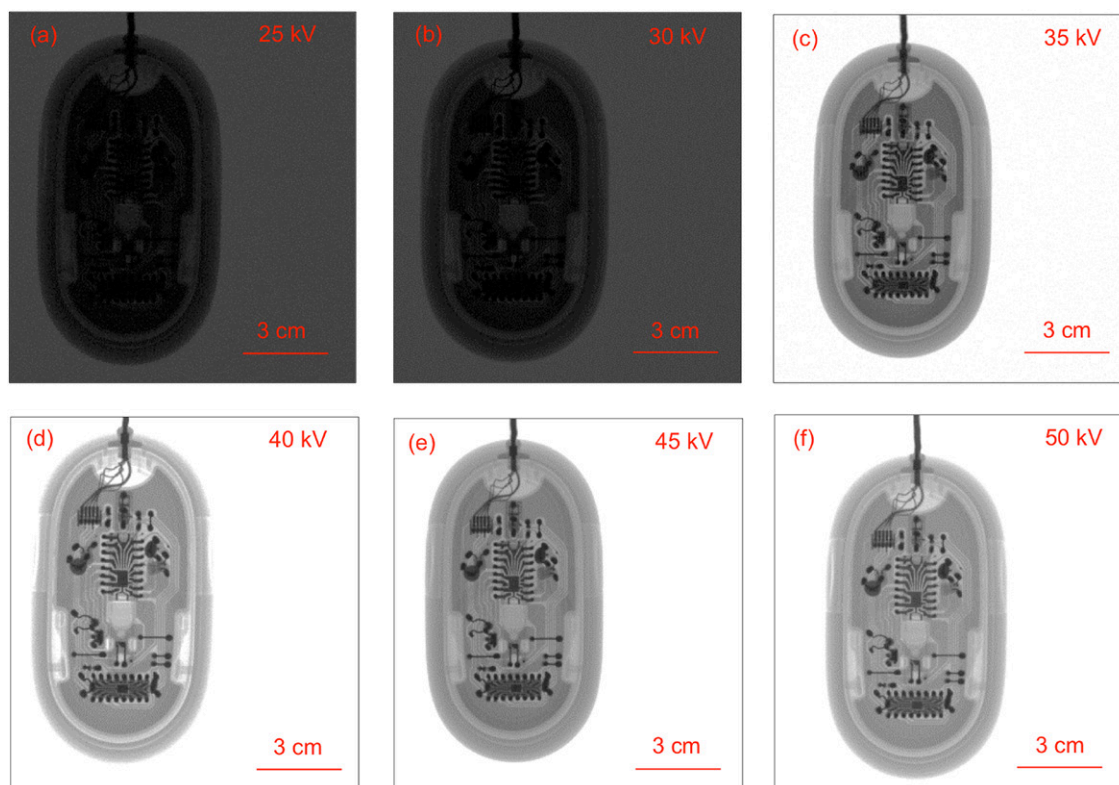
J. Phys. D: Appl. Phys. **48** (2015) 225501

A Basu *et al*

Figure 13. Absorption x-ray images of a computer mouse using $200\,\mu$A with $25\,$kV (*a*), $30\,$kV (*b*), $35\,$kV (*c*), $40\,$kV (*d*), $45\,$kV (*e*) and $50\,$kV (*f*) anode bias voltage.
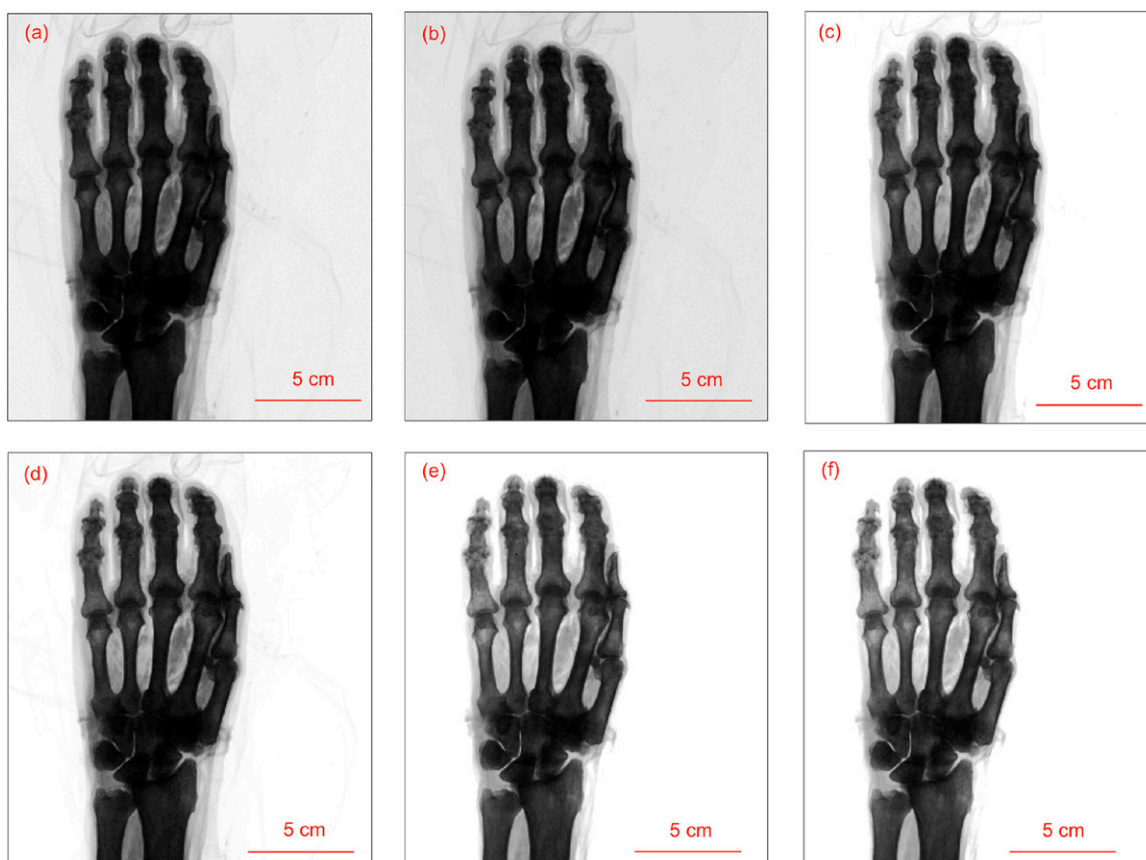

Figure 14. Absorption x-ray images of *ex vivo* human hand captured with anode bias voltage equal to $35\,$kV and cathode current equal to $150\,\mu$A (*a*), $200\,\mu$A (*b*), $250\,\mu$A (*c*), $330\,\mu$A (*d*), $400\,\mu$A (*e*), and $450\,\mu$A (*f*).

concluded that at around 35 kV anode bias voltage, the characteristic K_α-shell molybdenum peak reaches a maximum in terms of fraction of the total photons emitted, suggesting that a more monochromatic photon beam yields better absorption imaging. The images of the mouse at 35 kV anode bias voltage and above show the layout of the PCB as well as the leads and wires. The smallest features in the images are the interconnect wires on the PCB, which are distinctly visible. The resolution of the image is limited by the pixel size of the detector (~160 μm) and we estimate the size of the wires to be on the order of the pixel size.

Images of an *ex vivo* human hand were captured at various cathode currents and anode bias voltage of 35 kV (figure 14). Here again, the imaging mode is fluoroscopic with a 60 s exposure at 2 frames s^{-1} followed by frame averaging. While the metacarpus and phalanges are visible in all the images, the contrast between the low-Z muscle fibers and high-Z bone structures is better with increased dosage (at 250 μA and above). Comparing the image of the same *ex vivo* sample in [10] with those from figure 13, the porosity of the bones is more clearly visible in the former. However, the soft tissue structures, e.g. muscle fibers, are clearer in these images for cathode currents above 250 μA, suggesting that a Mo anode is better than a Au anode for imaging low-Z materials.

The x-ray source is capable of operating continuously for long periods of exposure, evidencing the stability of the system. Also, an absorption image captured with 250 μA cathode current for 60 s is equivalent to a dosage of 15 mA-s, which is of the same order required for radiographic absorption imaging with state-of-the-art x-ray sources (anywhere between 10–50 mA.s [39]). However, the cathodes in many x-ray sources used for imaging are capable of emitting tens of mA thereby reducing the required exposure time to a fraction of a second, which is highly desirable to avoid blurring the image due to movement of the patient. Nonetheless, the x-ray source described here could eventually reach that performance; the cathode chip technology has been shown capable of emitting three-orders-of-magnitude larger currents than what was used in these experiments [31]; in order to be compatible with such large thermal loads, the x-ray source would require better pumping capacity and active cooling, the latter either using deionized water to be compatible with the high-voltage anode or using less purified water with a grounded anode and a floating cathode.

6. Conclusion

A portable x-ray generator that uses a nanostructured, silicon-based, self-aligned FEA as electron source and a natural convection-cooled reflection Mo-coated Cu anode was reported. The cathode was shown to emit 1 mA current with <150 V during almost 20 h with no degradation and over 95% transmission. The x-ray spectra showed three characteristic peaks corresponding to the K-shell transitions of Cu and Mo. The source was shown to emit 3.39×10^8 17.4 keV photons μA^{-1} s^{-1} at an anode bias voltage equal to 35 kV, which maximizes the characteristic K_α-shell Mo peak. Fluoroscopic images of a computer mouse and an *ex vivo* human hand were captured at different anode bias voltages and cathode currents, demonstrating that absorption images captured using the optimal anode bias voltage for maximization of the x-ray fluorescence yield better contrast. Feature sizes as small as 160 μm were resolved in these images.

References

[1] Röntgen W C 1896 *Science* **3** 227
[2] Smyth M S and Martin J H J 2000 *Mol. Pathol.* **53** 8
[3] Stickle W F, Sobol P E and Bomben K D 1992 *Handbook of X-Ray Photoelectron Spectroscopy* vol **40** (Eden Prairie, MN: Perkin Elmer)
[4] Heuberger A 1988 *J. Vac. Sci. Technol.* A **6** 107
[5] Bethe H A and Heitler W 1934 *Proc. R. Soc. Lond. Ser.* A **146** 83
[6] Bugaev A S, Eroshkin P A, Romanko V A and Sheshin E P 2013 *Phys.—Usp.* **56** 691–703
[7] Neculaes V B, Edic P M, Frontera M, Caiafa A, Wang G and De Man B 2014 *IEEE Access* **2** 1568–85
[8] Gomer R 1961 *Field Emission and Field Ionization* (Cambridge, MA: Harvard University Press)
[9] Swanwick M E, Keathley P D, Fallahi A, Krogen P R, Laurent G, Moses J, Kärtner F X and Velásquez-García L F 2014 *Nano Lett.* **14** 5035–43
[10] Cheng S, Hill F A, Heubel E V and Velásquez-García L F 2015 *J. Microelectromech. Syst.* **24** 373–83
[11] Schwoebel P R, Boone J M and Shao J 2014 *Phys. Med. Biol.* **59** 2393
[12] Gidcumb E, Gao B, Shan J, Inscoe C, Lu J and Zhou O 2014 *Nanotechnology* **25** 245704
[13] Wang S, Calderon X, Peng R, Schreiber E C, Zhou O and Chang S 2011 *Appl. Phys. Lett.* **98** 213701
[14] Teo K B K *et al* 2003 *Nanotechnology* **14** 204
[15] Eletskii A V 2010 *Phys.—Usp.* **53** 863–92
[16] Ding M, Kim H and Akinwande A I 2000 *IEEE Electron Device Lett.* **21** 66
[17] Velásquez-García L F, Guerrera S, Niu Y and Akinwande A I 2011 *IEEE Trans. Electron Devices* **58** 1775
[18] Velásquez-García L F, Guerrera S, Niu Y and Akinwande A I 2011 *IEEE Trans. Electron Devices* **58** 1783–91

J. Phys. D: Appl. Phys. **48** (2015) 225501

A Basu *et al*

[19] Gasdaska C J, Falkos P, Hruby V, Robin M, Demmons N, McCormick R, Spence D and Young J 2004 *40th AIAA/ASME/SAE/ASEE Joint Propulsion Conf. and Exhibit* (*Fort Lauderdale, Florida, 11–14 July 2004*) AIAA 2004–3427

[20] Boone J M and Seibert J A 1994 *Med. Phys.* **21** 1853

[21] Dilmanian F A, Wu X Y, Parsons E C, Ren B, Kress J, Button T M and Zhong Z 1997 *Phys. Med. Biol.* **42** 371

[22] Dilmanian F A 1992 *Am. J. Physiol. Imaging* **7** 175–93

[23] Lopes R T, Costa E B and de Jesus E F O 2000 *Appl. Radiat. Isot.* **53** 665

[24] Nguyen T, Lu X, Lee C J, Jung J H, Jin G H, Kim S Y and Jeon I 2014 *Rev. Sci. Instrum.* **85** 093110

[25] Carroll F E, Mendenhall M H, Traeger R H, Brau C and Waters J W 2003 *Am. J. Roentgenol.* **181** 1197

[26] Diop B and Binh V-T 2012 *Rev. Sci. Instrum.* **83** 094704

[27] Yoon K-H, Kwon Y M, Choi B-J, Son H H, Ryu C W, Chon K S, Park S H and Juhng S K 2012 *Invest. Radiol.* **47** 683–7

[28] Kalender W A 2014 *Phys. Med. Biol.* **59** R129

[29] Saltybaeva N, Jafari M E, Hupfer M and Kalender W A 2014 *Radiology* **273** 153

[30] Cho H M, Ding H, Ziemer B P and Molloi S 2014 *Phys. Med. Biol.* **59** 7211

[31] Fomani A A, Guerrera S A, Velásquez-García L F and Akinwande A I 2014 *IEEE Trans. Electron Devices* **61** 2538

[32] Batey J and Tierney E 1986 *J. Appl. Phys.* **60** 3136–45

[33] Habermehl S, Apodaca R T and Kaplar R J 2009 *Appl. Phys. Lett.* **94** 012905

[34] Spindt C A, Brodie I, Humphrey L and Westerberg E R 1976 *J. Appl. Phys.* **47** 5248

[35] Brodie I and Spindt C 1992 *Advances in Electronics and Electron Physics* (New York: Academic) pp 1–106

[36] Zafar S, Callegari A, Gusev E and Fischetti M V 2002 *IEEE Int. Electron Devices Meeting, (IEDM)* (*December 2002*) 517–20

[37] Buhr H, Büermann L, Gerlach M, Krumrey M and Rabus H 2012 *Phys. Med. Biol.* **57** 8231

[38] Drouin D, Couture A R, Joly D, Tastet X, Aimez V and Gauvin R 2007 *Scanning* **29** 92–101

[39] Aldrich J E, Duran E, Dunlop P and Mayo J R 2006 *J. Digital Imaging* **19** 126–31